Mimicking Antiferroelectrics with Ferroelectric Superlattices

*Chunhai Yin, Yaqi Li, Edoardo Zatterin, Dorin Rusu, Evgenios Stylianidis, Marios Hadjimichael, Hugo Aramberri, Jorge Iñiguez-González, Michele Conroy, and Pavlo Zubko**

Antiferroelectric oxides are promising materials for applications in high-density energy storage, solid-state cooling, and negative capacitance devices. However, the range of oxide antiferroelectrics available today is rather limited. In this work, it is demonstrated that antiferroelectric properties can be electrostatically engineered in artificially layered ferroelectric superlattices. Using a combination of synchrotron X-ray nanodiffraction, scanning transmission electron microscopy, macroscopic electrical measurements, and lateral and vertical piezoresponse force microscopy in parallel-plate capacitor geometry, a highly reversible field-induced transition is observed from a stable in-plane polarized state to a state with in-plane and out-of-plane polarized nanodomains that mimics, at the domain level, the nonpolar to polar transition of traditional antiferroelectrics, with corresponding polarization-voltage double hysteresis and comparable energy storage capacity. Furthermore, it is found that such superlattices exhibit large out-of-plane dielectric responses without involving flux-closure domain dynamics. These results demonstrate that electrostatic and strain engineering in artificially layered materials offers a promising route for the creation of synthetic antiferroelectrics.

1. Introduction

The recent revival of interest in antiferroelectrics is as much due to their technological potential as it is due to the many open questions that are as fundamental as the definition of antiferroelectricity itself.[1,2] Antiferroelectrics are usually described as materials with an antipolar ground state, which is sufficiently close in energy to a polar phase that a first-order transition into the polar state can be induced by an applied electric field.[3] The antipolar phase is characterised by oppositely oriented local electric dipoles that lead to an overall non-polar unit cell. Field-induced switching from this antipolar to the polar phase and the subsequent return to the antipolar state at zero field give rise to the characteristic double hysteresis in polarization-voltage curves that serves as a hallmark of antiferroelectricity. The steep polarization switching and complete discharge upon removal of the field make antiferroelectrics attractive candidates for high energy density capacitors, while the polarization hysteresis away from zero field opens the possibility for negative capacitance behavior at higher voltages than in ferroelectrics, thus providing an additional tuning parameter in the quest for lower-power field effect transistors.[4] Additionally, antiferroelectrics not only have large electrocaloric responses that could be exploited for solid state cooling,[5] but exhibit both signs of the electrocaloric effect.[6,7] However, despite these desirable properties, the palette of antiferroelectric materials at our disposal today remains limited, while at the same time the complex nature of antiferroelectricity means that our understanding of even the best-studied materials, such as lead zirconate, remains far from complete.[8–11]

C. Yin, Y. Li, E. Stylianidis, P. Zubko
Department of Physics and Astronomy
University College London
Gower Street, London WC1E 6BT, UK
E-mail: p.zubko@ucl.ac.uk

Y. Li, D. Rusu, M. Hadjimichael, P. Zubko
London Centre for Nanotechnology
17–19 Gordon Street, London WC1H 0HA, UK

The ORCID identification number(s) for the author(s) of this article can be found under https://doi.org/10.1002/adma.202403985

DOI: 10.1002/adma.202403985

E. Zatterin
ESRF
The European Synchrotron
71 Avenue des Martyrs, Grenoble 38000, France

M. Hadjimichael
Department of Physics
University of Warwick
Coventry CV4 7AL, UK

H. Aramberri, J. Iñiguez-González
Luxembourg Institute of Science and Technology (LIST)
Avenue des Hauts-Fourneaux 5, Esch/Alzette L-4362, Luxembourg

J. Iñiguez-González
Department of Physics and Materials Science
University of Luxembourg
Rue du Brill 41, Belvaux L-4422, Luxembourg

M. Conroy
Department of Materials
Imperial College London
Exhibition Road, London SW7 2AZ, UK

In this work we demonstrate that antiferroelectric-like properties can be electrostatically engineered in ferroelectric superlattices consisting of alternating ultrathin layers of $PbTiO_3$ and $SrTiO_3$. In recent years, ferroelectric-dielectric superlattices have proven to be an exciting platform for exploring nanoscale ferroelectricity. Under the strong influence of mechanical and electrostatic boundary conditions, the ferroelectric layers in such structures adopt exotic polarization configurations that are unattainable in bulk materials. The complex flux-closure patterns,[12,13] chiral bubble domains,[14] and 3D-ordered domain crystals[15,16] that appear in ferroelectric superlattices are highly responsive to applied fields and can give rise to giant enhancements of the dielectric susceptibility and negative capacitance effects.[17] Interestingly, the periodic arrangement of oppositely polarized nanoscale domains in many such structures bears some resemblance to the antipolar structure of antiferroelectrics, while the energetic proximity to a macroscopically polar state, which can be tuned by appropriate selection of the layer thicknesses, can also lead to pinched hysteresis.[18–20] Moreover, the depolarizing fields that favor the macroscopically non-polar multidomain ground state, can also be exploited to stabilize competing non-polar or antipolar phases that are otherwise unstable or metastable in the bulk material.[21–23]

Here we study $PbTiO_3/SrTiO_3$ superlattices deposited on $DyScO_3$ substrates. While previous work has focused largely on superlattice compositions with out-of-plane flux-closure-type polarization patterns,[13,24] we investigate structures where out-of-plane polarization is electrostatically suppressed. We show that at zero field such superlattices are fully in-plane polarized, except at charged superdomain boundaries, where an out-of-plane polarization appears to neutralize the polarization divergence. We then demonstrate that these superlattices exhibit highly reversible antiferroelectric-like switching from a robust in-plane polarized state at zero field to one with a finite out-of-plane component. Using a combination of synchrotron X-ray nanodiffraction and piezoresponse force microscopy (PFM), we show that this switching proceeds inhomogeneously through nucleation of out-of-plane polarized domains within the in-plane polarized superdomains. Finally, we show that despite being in-plane polarized, such superlattices have out-of-plane dielectric permittivities comparable to those where negative capacitance effects have been reported and attributed to nanoscale flux-closure domains (a.k.a. vortices).[25]

2. Structural Characterization

Superlattices consisting of periodic repetitions of 9 unit cells of $PbTiO_3$ and m unit cells of $SrTiO_3$ (denoted as $(9|m)$ hereafter), with and without top and bottom $SrRuO_3$ electrodes, were deposited on orthorhombic (110)-oriented $DyScO_3$ substrates using off-axis magnetron sputtering as described in the Methods section. The $PbTiO_3$ layer thickness was chosen to be below 10 unit cells to favor a state with an in-plane polarization and no out-of-plane flux-closure (vortex) domains.[24,26]

Figure 1a,b shows high angle annular dark field scanning transmission electronic microscopy (HAADF-STEM) images of a (9|4) superlattice at different magnifications, where the $PbTiO_3$ layers appear brighter than the $SrTiO_3$ layers due to the higher atomic number of Pb. The thickness of the lamella prepared using a focused ion beam was deliberately kept relatively large to avoid significant changes to the electrostatic and mechanical boundary conditions that are known to induce flux-closure domains not present in the original sample.[27] In-plane and out-of-plane strain maps obtained from Figure 1a using geometric phase analysis (GPA)[28] are shown in panel c. No lateral variation is observed in the out-of-plane strain map, consistent with a uniform average out-of-plane lattice parameter within each layer (with our chosen GPA parameters, the difference between $SrTiO_3$ and $PbTiO_3$ is not resolved here). By contrast, the map of in-plane strain (η_{xx}) shows stripe-like regions with alternating extended and compressed lattice parameter, as expected from in-plane polarized a_1/a_2 domains with polarization along [100] and [010] pseudocubic (pc) directions, and {110}-oriented domain walls viewed here in projection along the [010] zone axis (we note that these projections and the lattice tilts associated with tetragonal twinning make it difficult to accurately quantify local strains or extract atomic dipole maps from our HAADF images).

The in-plane polarized state can also be inferred from synchrotron X-ray diffraction (XRD) reciprocal space mapping (see Methods). Reciprocal space maps (RSMs) obtained around the off-specular 103_{pc} reflection show periodic satellites characteristic of a_1/a_2 domains, as illustrated for the (9|4) superlattice in Figure 1d. In this sample, a strong preference for $(\bar{1}10)_{pc}$ domain walls over $(110)_{pc}$ domain walls is evident from the q_y-q_x projection, which may be due to either (or a combination of) the orthorhombic structure of the substrate or the direction of its surface miscut.[29] The domain period obtained from the satellite positions is around 60 nm. In all samples, the domain sizes are substantially larger than the superlattice periods, indicating that the ferroelectric layers are mechanically coupled and implying that the a_1/a_2 domain walls extend over many (if not all) periods of the superlattice.

XRD $\theta-2\theta$ scans for four samples shown in Figure S1 (Supporting Information) reveal a single set of well-defined superlattice peaks (Figure S1, Supporting Information), as expected for a purely in-plane polarized state.[24] However, in some cases a very weak additional set of peaks accompanied by in-plane domain satellites can be discerned in the RSMs (e.g., in Figure S2, Supporting Information), suggesting a trace of out-of-plane flux-closure domains. Unexpectedly, a much stronger set of sharp a_1/a_2 domain satellites with the same periodicity as those around the 103_{pc} peaks is also observed around certain specular superlattice reflections and/or at reciprocal space positions between the structural superlattice peaks (Figure S2, Supporting Information). We attribute these to hybrid reflections caused by multiple scattering[30] rather than a modulated out-of-plane polarization component.[31]

3. Domain Structure at Zero Bias

To image the a_1/a_2 superdomain structure, we perform PFM measurements on superlattice capacitors with top and bottom $SrRuO_3$ electrodes as described in the Methods section and illustrated in **Figure 2a**. Figure 2b,c shows the lateral PFM amplitude and phase images obtained on the (9|4) superlattice capacitor; despite the presence of the top electrode, periodic a_1/a_2 domain stripes are clearly resolved.

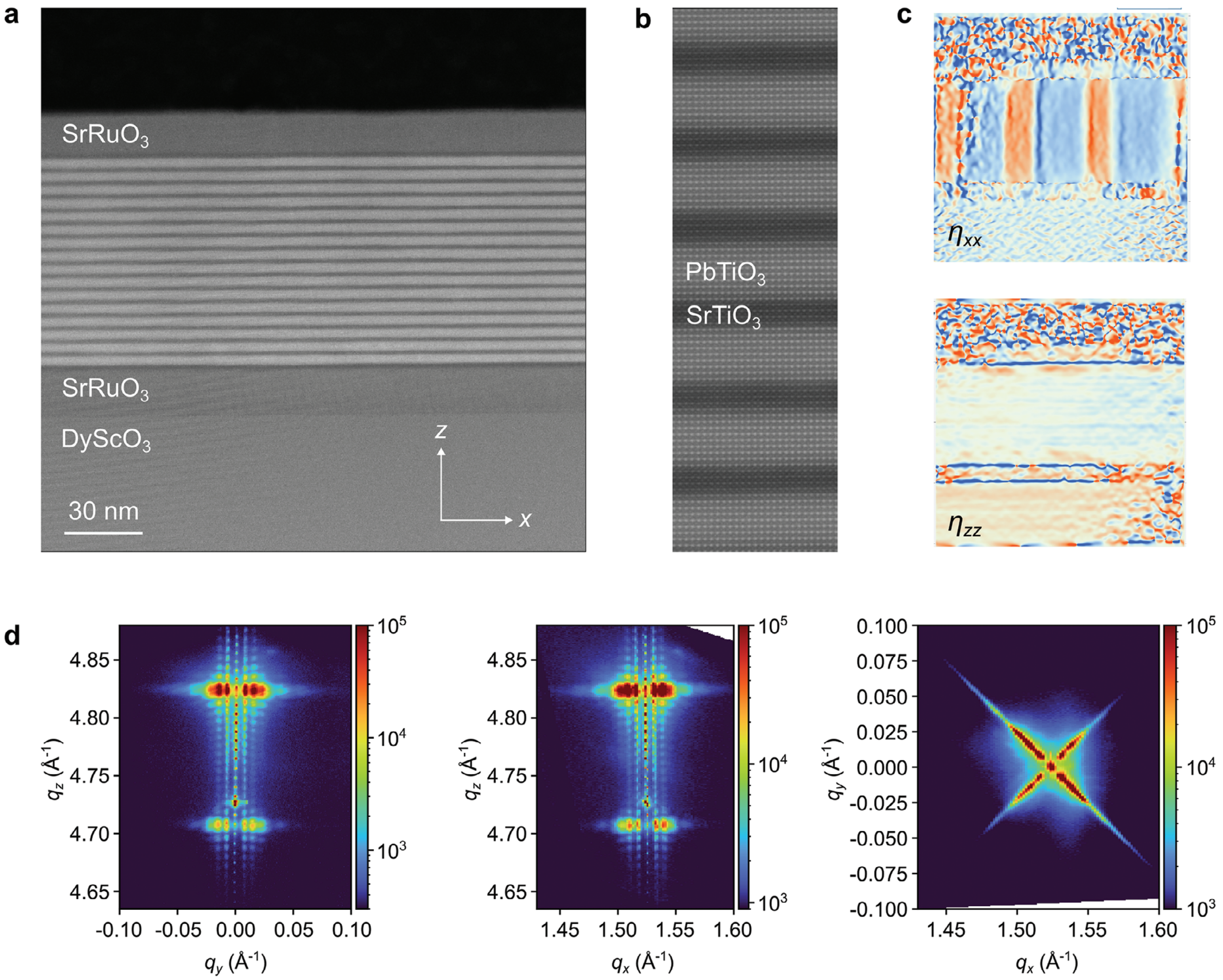

Figure 1. Structural characterization of in-plane polarized superlattices. a) Cross sectional STEM HAADF image of the (9|4) superlattice with top and bottom SrRuO$_3$ electrodes deposited on a (110)$_o$ DyScO$_3$ substrate. b) Higher magnification image of the superlattice showing the PbTiO$_3$ layers (bright) and SrTiO$_3$ layers (dark). c) In-plane strain η_{xx} and out-of-plane strain η_{zz} distributions obtained from GPA of image in (a). d) Three projections of the diffracted intensity within a 3D reciprocal space volume around the 103$_{pc}$ reflections showing the superlattice periodicity along q_z and the satellites along the ⟨110⟩$_{pc}$ directions due to a$_1$/a$_2$ domains with a period of approximately 60 nm.

Figure 2 panels d to i and Figure S3 (Supporting Information) show the lateral (L) and vertical (V) PFM images obtained over a larger region of the same sample for two orthogonal cantilever orientations. In these measurements the cantilever and image edges are at approximately 10° relative to the pseudocubic ⟨110⟩ directions. Therefore regions with the largest LPFM amplitude in panel e correspond to superdomains with a net polarization along [110] and [$\bar{1}\bar{1}$0], while those in panel f correspond to superdomains with net polarization along [1$\bar{1}$0] and [$\bar{1}$10]. Combining the amplitude and phase information for the two orthogonal cantilever orientations allows us to reconstruct the superdomain polarization arrangement, as shown in Figure 2k.

Interestingly, while the VPFM images in panels d and g exhibit little contrast within the a$_1$/a$_2$ superdomains as expected, we observe some enhancement of the vertical piezoresponse near the a$_1$/a$_2$ superdomain boundaries, suggesting the possible presence of out-of-plane polarization there. Superimposing the normalized VPFM amplitude (above a threshold value of 0.2) on the LPFM data (see panel k), reveals that the VPFM signal appears at nominally "charged" boundaries where the net superdomain polarizations meet head-to-head (H-H) or tail-to-tail (T-T). This suggests that the out-of-plane polarization at these boundaries appears in order to avoid a polarization divergence in the same way as for the so-called polar merons reported in PbTiO$_3$ on GdScO$_3$.[32] We find that oppositely "charged" boundaries give rise to opposite orientations of the out-of-plane polarization, as can be deduced from the sign reversal of the VPFM phase in Figure 2g. Similar VPFM response has recently been observed at charged domain walls in uniaxial ferroelectrics and attributed to counteracting effects of shear strain at the boundary between oppositely poled domains, an effect that could also be at play here.[33] Parenthetically, we note that the change in sign of the

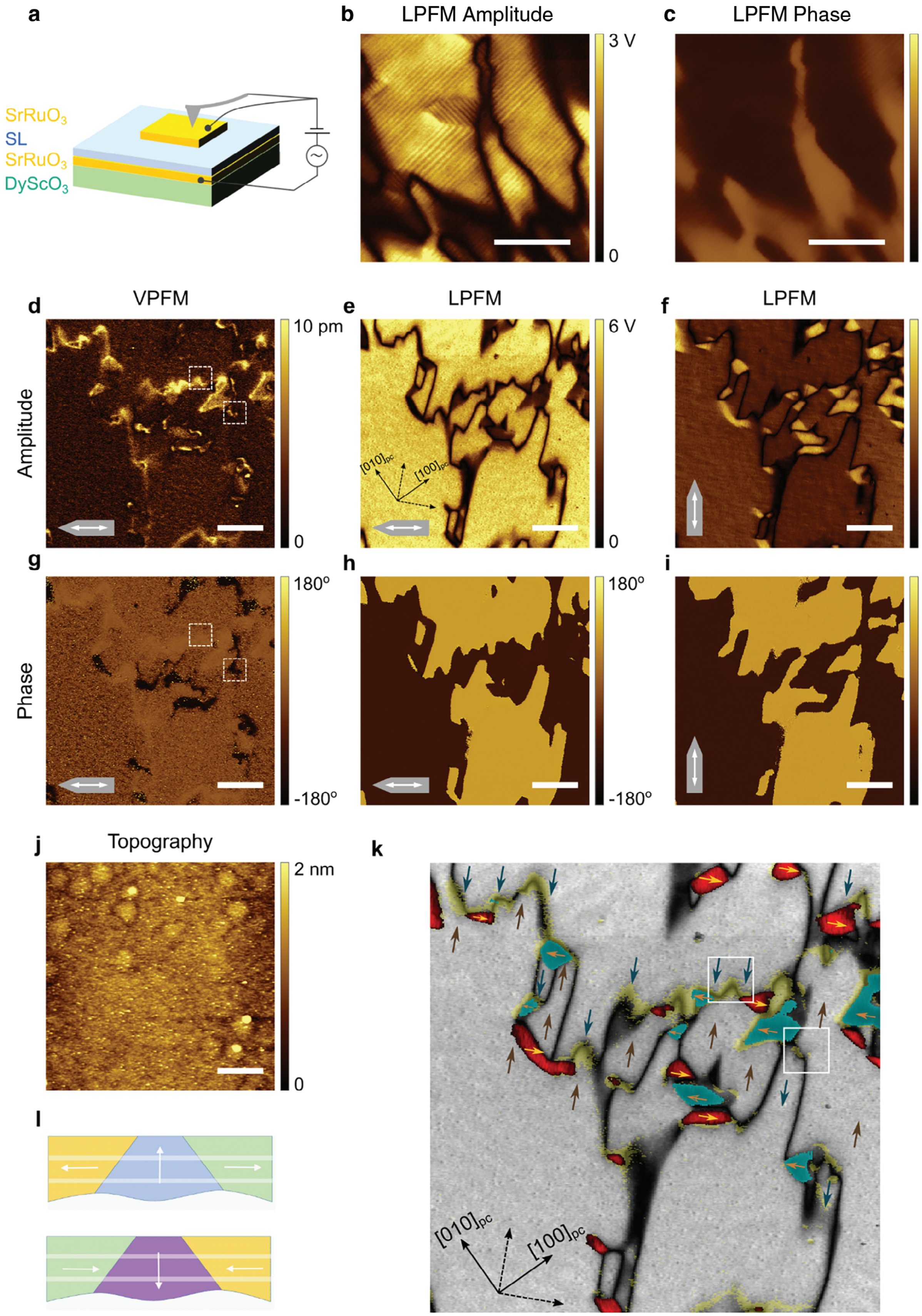
a
$SrRuO_3$
SL
$SrRuO_3$
$DyScO_3$
b
LPFM Amplitude
3 V
0
c
LPFM Phase
d
VPFM
Amplitude
10 pm
0
e
LPFM
6 V
0
$[010]_{pc}$
$[100]_{pc}$
f
LPFM
g
Phase
180°
-180°
h
180°
-180°
i
j
Topography
2 nm
0
k
$[010]_{pc}$
$[100]_{pc}$
l

vertical polarization component along the superdomain boundaries is reminiscent of the "domains within domain walls" picture discussed by Salje et al.[34]

Our combined STEM, XRD and PFM characterization thus reveals that, except at nominally charged superdomain boundaries, where some out-of-plane polarization is observed, and a negligibly small fraction of periodic out-of-plane flux-closure domains, our (9|m) superlattices are essentially in-plane polarized with a periodic a_1/a_2 domain structure. This is in contrast to $PbTiO_3$ films on $DyScO_3$, which usually display a/c domains.[35] We attribute the suppression of the out-of-plane polarization components in our $PbTiO_3$ layers to the large electrostatic penalty associated with depolarizing fields that would arise at interfaces between the $PbTiO_3$ and $SrTiO_3$ layers in the superlattice. Interestingly, such "incipient ferroelectric" superlattices with an electrostatically suppressed out-of-plane polarization component are predicted to exhibit enhanced negative capacitance, which serves as a further motivation for our study.[36]

4. In-Plane Ferroelectric and Out-of-Plane Antiferroelectric-Like Switching

Next, we investigate the electrical properties of our superlattices, beginning with the in-plane response measured using a co-planar interdigitated electrode pattern (see Methods). Capacitance-voltage measurements for the (9|6) superlattice (**Figure 3a**) at room temperature show the typical ferroelectric butterfly loop, as expected for in-plane polarized $PbTiO_3$. At lower temperature (not shown here), the coercive field increases and becomes inaccessible with our maximum applied voltage (40 V). For reference, the behavior of pure $SrTiO_3$ films on $DyScO_3$ was also studied and is consistent with previous reports of strain-induced ferroelectric-like behavior, as shown in Figure S4 (Supporting Information).

Figure 3b shows the temperature dependence of the out-of-plane relative dielectric permittivity ϵ_{zz} and loss tangent (tan δ) obtained in parallel-plate capacitor geometry for different (9|m) superlattices. The permittivity decreases monotonically as the temperature is reduced for all but the (9|10) sample, which shows a broad peak. The permittivity-voltage and corresponding loss tangent-voltage curves are shown in Figure 3c for the (9|4) samples and in Figure S5 (Supporting Information) for the remaining superlattices. At all temperatures from 300 to 15 K, $\epsilon_{zz}(V)$ measurements for the (9|10) sample (Figure S5, Supporting Information) show almost hysteresis-free curves with moderate tuneability, as expected for a non-linear dielectric with no out-of-plane ferroelectricity. However, the behavior of the (9|4) and (9|3) samples is qualitatively different. At room temperature, the permittivity of the (9|4) superlattice (Figure 3c) is approximately constant up to ± 2.5 V. It then increases slightly, peaking at around 3.5–4 V, before dropping sharply at higher voltages. Only weak hysteresis is observed upon cycling. The polarization-voltage characteristics (Figure 3d; Figure S6, Supporting Information) are overall quite linear, with a small kink at around 4 V and narrow hysteresis. At 15 K, the sample exhibits highly reversible, non-hysteretic and weakly tuneable $\epsilon_{zz}(V)$ curves up to approximately 2.5 V. For larger bias, however, a hysteretic drop in permittivity is observed. *P–V* measurements at 15 K yield a pronounced double hysteresis loop, characteristic of antiferroelectric materials.

We note that pinched or double hysteresis can also arise in ferroelectrics for a number of reasons, e.g. near first-order ferroelectric phase transitions or due to domain pinning by defects.[37–39] However, the mechanism at play here is quite different. At zero field, our superlattices always return to a state with negligible out-of-plane polarization and show highly reversible P-V characteristics at low fields, which can be attributed to the strong restoring force provided by the depolarization field that drives the system to a purely in-plane polarized state at zero field. At high fields, the hysteretic jump in the out-of-plane polarization is related to the latent out-of-plane polarization that would appear in a perfectly screened $PbTiO_3$ films at the strain state provided by the $DyScO_3$ substrate.[36,40] Thus, at sufficiently high bias, the out-of-plane component can be stabilized and results in the observed hysteresis. To investigate the mechanism by which this out-of-plane polarization develops, we turn to synchrotron X-ray nanodiffraction and PFM imaging.

5. Domain-Structure Evolution Under Applied Field

Figure 4a shows the intensity distribution within a 3D reciprocal space volume around the 103_{pc} reflection for the (9|4) superlattice capacitor at 10 V applied bias. Its projections onto different planes in reciprocal space are shown in Figure 4b. Comparison with the RSMs at 0 V (Figure 1d) reveals the presence of additional X-shaped diffuse intensity features characteristic of tilted a/c domains.[35] To probe the spatial distribution of these features on the sample, we position the detector so that it simultaneously captures the features from both a_1/a_2 periodicities, two of the four possible a/c domain tilts and the $SrRuO_3$ electrodes, as shown in Figure 3c; the corresponding surface in reciprocal space is highlighted in Figure 3a. We then scan the sample relative to the beam and record the intensities in the regions of interest (roi) centred on each of the above features as a function of position on the

Figure 2. PFM imaging of a_1/a_2 domains and vertical piezoresponse at superdomain boundaries. a) Sketch of the setup for PFM measurements through the top electrode. b,c) LPFM amplitude and phase images revealing the periodic a_1/a_2 stripe domains; the scale bar corresponds to 1 µm. d–i) Lower magnification VPFM and LPFM amplitude and phase images obtained for two orthogonal cantilever orientations relative to the sample. The cantilever orientations and scan directions are shown as insets in each image. j) Sample topography (scale bar is 2 µm). k) Composite image consisting of the LPFM amplitude response in (e) in grayscale, overlaid with a thresholded VPFM amplitude image (d) in green and high amplitude regions in (f) colored by the corresponding phase from (i); see Methods for more details. Colored arrows indicate the net superdomain polarization orientations deduced from the two sets of orthogonal LPFM images. As the absolute direction of the polarization cannot be determined, an alternative pattern with all the directions reversed is also consistent with the data. Black arrows indicate the approximate pseudocubic crystallographic directions. The image shows that regions with maximum out-of-plane piezoresponse in (d) correspond to nominally "charged" boundaries where the superdomain polarizations meet head-to-head (H-H) and tail-to-tail (T-T). The phase of the VPFM response is opposite for H-H and T-T boundaries (e.g., see areas highlighted by white boxes), indicating opposite orientations of the out-of-plane polarization components. l) Sketch of two of the possible polarization arrangements at the H-H and T-T superdomain boundaries across the first few periods of the superlattice.

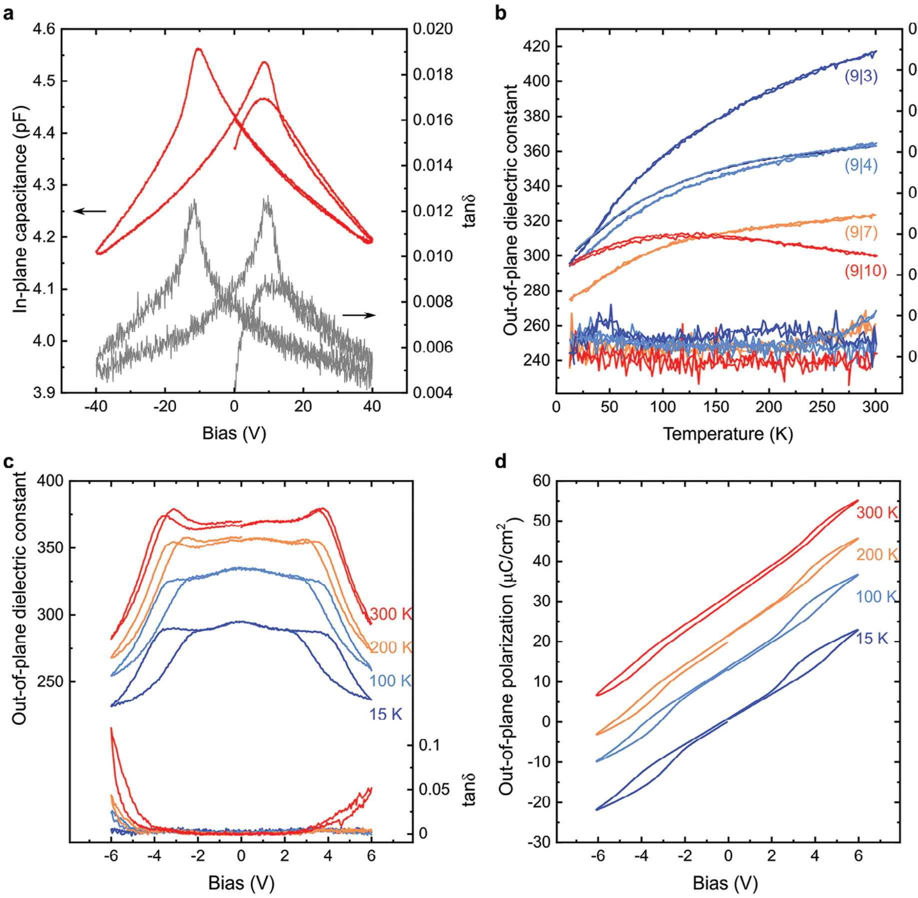

Figure 3. Electrical properties of in-plane polarized superlattices. a) In-plane capacitance-voltage characteristics of a (9|4) superlattice at room temperature obtained using co-planar interdigitated electrodes. A butterfly loop typical of ferroelectric switching is observed. b) Temperature dependence of the out-of-plane effective permittivity measured in parallel-plate capacitor geometry for (9|m) superlattices. c) Relative permittivity- and loss tangent-voltage, and d) polarization–voltage curves at selected temperatures for the (9|4) superlattice demonstrating antiferroelectric-like behavior. The polarization–voltage curves at different temperatures have been offset vertically for clarity.

sample probing an area at the edge of a circular top electrode (see Methods). The results are presented in Figure 3d.

At zero bias, only a_1/a_2 domain signatures are clearly visible, with the dominant a_1/a_2 domain variant appearing in roi2 and the minority variant in roi1. As the bias is increased, there are no noticeable changes in the positions of the a_1/a_2 superdomain boundaries but the intensity of the a_1/a_2 features under the electrode decreases, while new intensity appears in roi7 and roi8 corresponding to two of the four possible c-domain tilts. The intensity changes appear rather uniform on a scale of many microns, implying that the individual a/c superdomains that nucleate under applied field are smaller than our resolution, which is limited by the beam footprint (about 78 nm at this angle of incidence). The original zero-bias domain structure is fully restored when the field is removed.

Figure 5 illustrates the evolution of the vertical and lateral piezoresponse with applied DC bias. As the magnitude of the DC bias increases, vertical piezoresponse signal appears within the a_1/a_2 superdomain regions indicating the nucleation of out-of-plane polarized c domains there. At 4 V, coincident with the sharp drop in capacitance in Figure 3c, the domain pattern transforms into a coexistence of a_1/a_2 domains and a regular network of c-domains. The appearance of these c-domains is consistent with the appearance of inhomogeneous lattice tilts observed in diffuse scattering measurements in Figure 4.

Thus, our X-ray nanodiffraction and PFM measurements demonstrate that the mechanism behind the AFE-like switching involves the nucleation of out-of-plane polarized domains within the a_1/a_2 superdomains and their subsequent disappearance upon removal of the field. The process is highly inhomogeneous with an identical domain pattern induced upon subsequent application of field, and complete restoration of the exact original a_1/a_2 superdomain structure upon removal of the field, as shown in Figure S7 (Supporting Information) and consistent with the nanodiffraction data. We note that although field-induced conversion between a_1/a_2 and a/c structures can also be observed in thin films of $PbTiO_3$ under tensile strain,[41–43] such switching usually leads to remanence (i.e., the field-induced phases remain metastable at zero field over long periods of time). This is because such structures lack an efficient restoring force for the a_1/a_2 structure, which in our case is provided by depolarization effects due to the $SrTiO_3$ spacers.

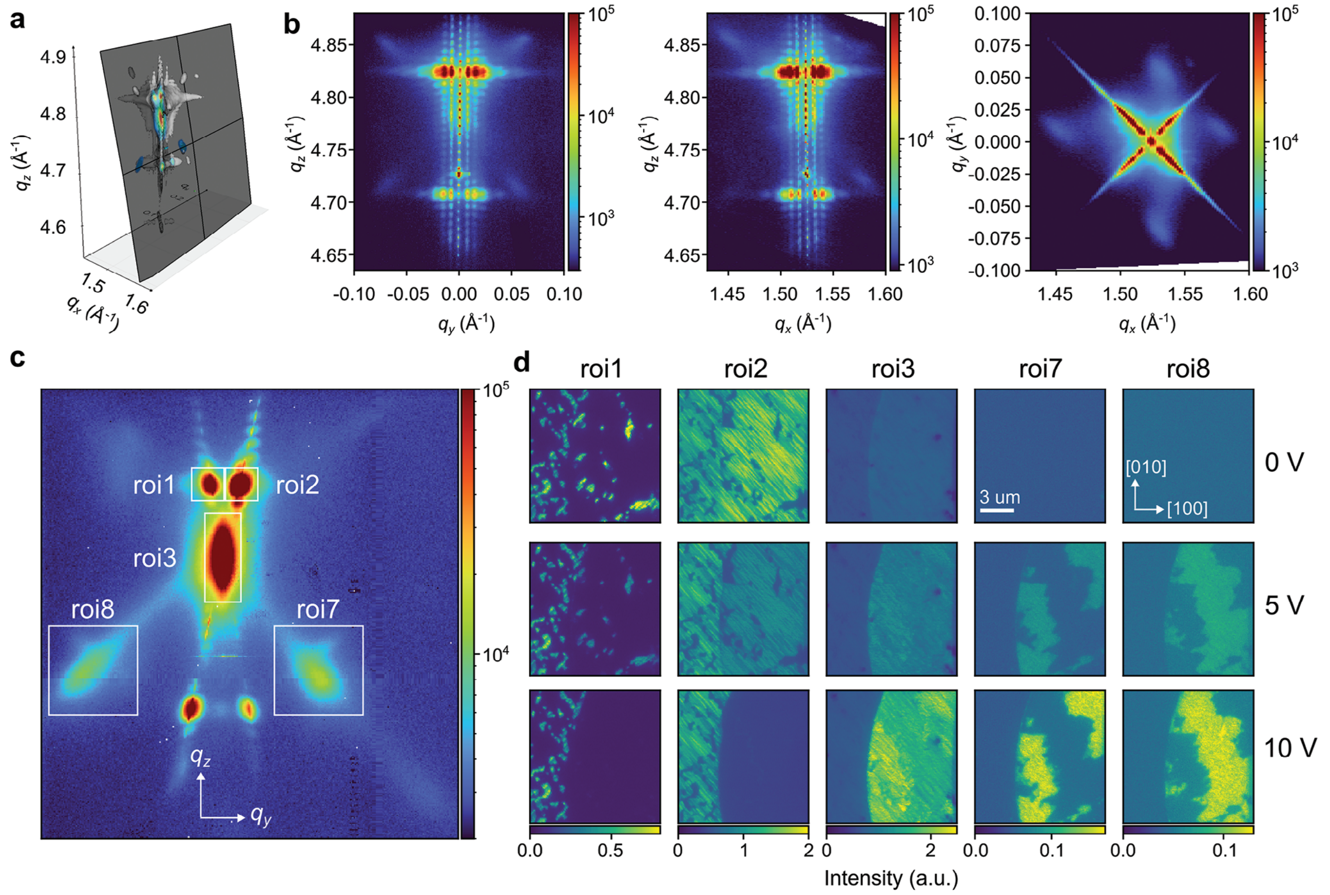

Figure 4. Synchrotron X-ray nanodiffraction with in-situ biasing. a) Diffracted intensity in a 3D reciprocal space volume around the 103_{pc} reflection of the substrate at 10 V applied bias. b) 2D projections of the diffracted intensity in (a) onto different planes in reciprocal space. c) Intensity distribution on the detector at the position used for the nanodiffraction imaging with regions of interest highlighted as boxes. The corresponding surface in reciprocal space is highlighted in (a). d) Intensity in the different regions of interest as a function of position on the sample for different applied voltages obtained by scanning the sample relative to the beam. Roi1 and roi2 correspond to the two orthogonal periodicities of the a_1/a_2 superdomains (minority and majority variants, respectively), while roi7 and roi8 correspond to two of the four possible lattice tilts of the field-induced c domains. The edge of the circular electrode is most clearly visible at all voltages in roi3, which contains the signal from the $SrRuO_3$ layers. The intensity of features from the periodic a_1/a_2 domains under the electrode decreases with applied bias, while that from the tilted c domains increases. Measurements in panels a-c were performed with a wide beam, while a nanofocused beam was used for the measurements in (d). See Methods for details.

6. Atomistic and Phase-Field Simulations

To verify our picture of the switching process and visualize how the out-of-plane polarization emerges from the purely in-plane polarized state, we perform atomistic and phase-field simulations as described in Methods. The results of our second-principles atomistic simulations for (10|4) and (10|6) superlattices subjected to different levels of tensile strain are summarized in Figure S8 (Supporting Information). At 0% strain, the superlattices exhibit out-of-plane polarized stripe domains that give rise to pinched or double hysteresis loops during field cycling, as discussed elsewhere.[18–20] For tensile strains of 1% and above, the zero-field state is purely in-plane polarized, as we observe experimentally. However, the lateral dimensions of our calculation cell (we checked up to 8 uc x 16 uc) preclude the formation of a_1/a_2 domains, resulting in a monodomain state with polarization along $[110]_{pc}$. Under applied field, the polarization rotates continuously in a non-hysteretic manner, indicating that more complex domain structures are required to explain the experimentally observed behavior.

To access these larger-scale domain structures, we perform phase-field simulations. Rather than tackling the full complexity of the coupled layers in a superlattice, we attempt to capture the essential physics of the interplay between strain and electrostatics within a single $PbTiO_3$ layer as follows. First, we adjust the model parameters as described in the Methods section so as to stabilize the $a_1/a_2/c$ domain structure (**Figure** 6a) in a 10 u.c. thick $PbTiO_3$ layer under short-circuit boundary conditions, thus mimicking the behavior of fully screened $PbTiO_3$ film on $DyScO_3$. This state serves as a reference for the domain structure expected from strain alone, i.e., in the absence of depolarization effects.

Next, to model the electrostatics of the superlattices, we sandwich this $PbTiO_3$ layer between two dielectric spacers with an arbitrarily chosen dielectric constant of 100. The results are summarized in Figure 6b. At zero field, the structure relaxes to a

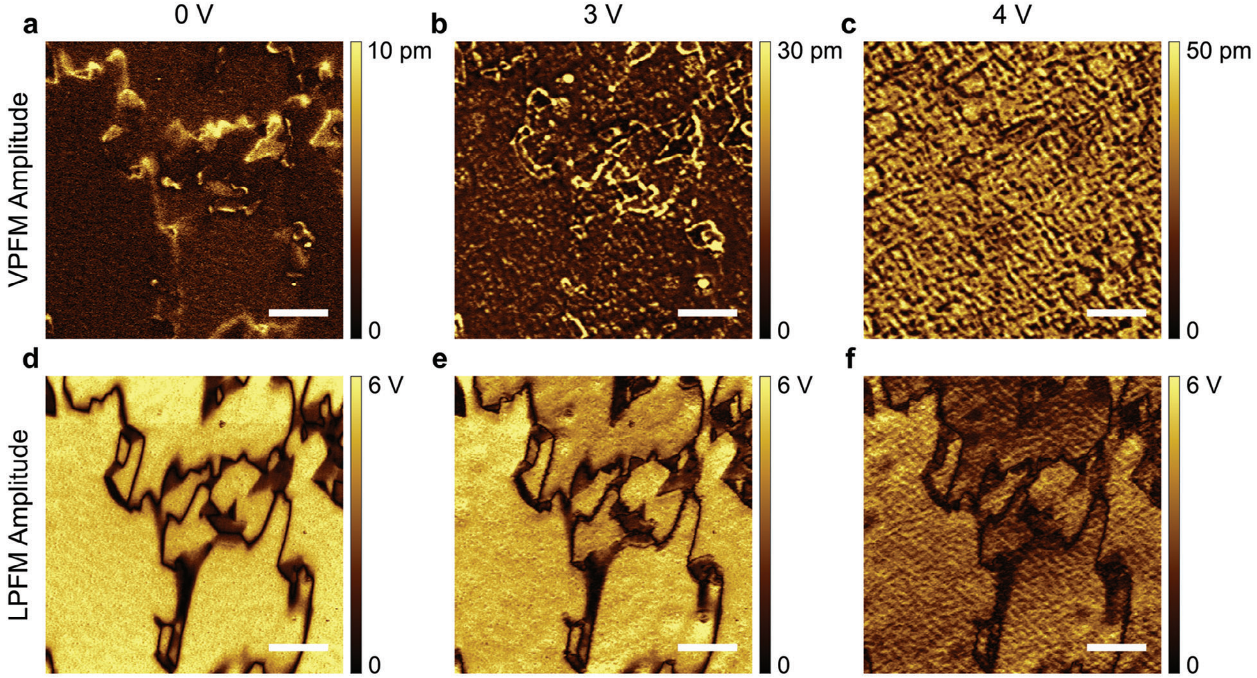

Figure 5. Domain structure evolution under DC bias. Vertical (a–c) and lateral (d–f) PFM amplitude images at 0, 3, and 4 V DC bias. At 0 V, VPFM signal is observed only at superdomain boundaries. At 3 V, the signal at superdomain boundaries is enhanced and nucleation of domains with weak VPFM response is visible within the superdomains. At 4 V, regions with strong VPFM response are visible everywhere. These regions are elongated approximately along the pseudocubic axes, as expected for a/c-type domain structure. A corresponding reduction in the LPFM amplitude is observed, but overall, the a_1/a_2 superdomain structure is preserved and recovers fully if the bias is switched off. The scale bar corresponds to 2 µm.

single a_1/a_2 superdomain with multiple individual domains. Thus the a/c domain structure favored by strain alone is now suppressed to avoid the depolarizing field associated with a finite out-of-plane polarization. Parenthetically, we note that the a_1/a_2 superdomains have a net polarization perpendicular to the domain walls and an anti-polar arrangement of polarization parallel to the domain walls, bearing some resemblance to antiferroelectric $K_3Nb_3B_2O_{12}$, which has an antipolar arrangement of dipoles that are canted to produce a net polarization perpendicular to the antipolar order.[44]

Subsequent application of bias leads to the nucleation of c-domains, as illustrated in Figure 6b, where the domain structure at 9 V consists of a mixture of a and c domains. Reducing the bias to zero again restores the original a_1/a_2 structure. Although the exact details of the domain structure depend on the choice of model parameters, the qualitative behavior is robust and our phase field calculations of a $PbTiO_3$ layer with a single a_1/a_2 superdomain variant already capture the main experimentally observed features of our superlattices, namely that: (i) the zero-field a_1/a_2 state appears due to the depolarization-induced suppression of c-domains with out-of-plane polarization; and (ii) the a/c-domain state, which is favored by strain, can be induced by application of a field.

7. Implications for Energy Storage and Negative Capacitance

From our hysteresis loops, we can compute the recoverable energy stored in our capacitors, which at room temperature and 550 kV cm^{-1} is ≈ 6 J cm^{-3}, comparable to many good antiferroelectric materials.[45] It is likely that the energy storage capacity could be further optimized through a systematic study of different superlattice compositions.

As regard a potential negative-capacitance behavior of these superlattices, unfortunately, the method for extracting individual layer permittivities employed in ref. [17], which relies on a simple electrostatic model of the total capacitance as a function of thickness of the $SrTiO_3$ layer, cannot be applied here for two reasons. First, $SrTiO_3$ under tensile strain undergoes a ferroelectric transition with associated finite size effects.[46] Second, the $SrTiO_3$ layers in our superlattices are further distorted by the elastic coupling to the in-plane polarized $PbTiO_3$ layers, which may push their ferroelectric T_c above room temperature. While the likely appearance of in-plane ferroelectricity in our $SrTiO_3$ layers will not contribute to the depolarizing field effects along the out-of-plane direction, it does mean that the permittivity of the $SrTiO_3$ layers cannot be assumed to be independent of their thickness and cannot be directly compared to that of $SrTiO_3$ thin films on $DyScO_3$ substrates. Therefore, no conclusive evidence for the presence or absence of negative capacitance in the $PbTiO_3$ layers can be extracted for superlattices on $DyScO_3$ from our data. However, it is interesting to note that the room-temperature effective permittivity of our (9|7) and (9|10) superlattices (≈300–320) is similar to that of the (12|12) superlattice with a mixture of flux-closure (vortex) and a_1/a_2 domains studied by Yadav et al.[25] (ϵ_r ≈ 375), where negative capacitance behavior was inferred and attributed to the field-induced response of the vortices. Barring a coincidental agreement (we note that our samples are deposited

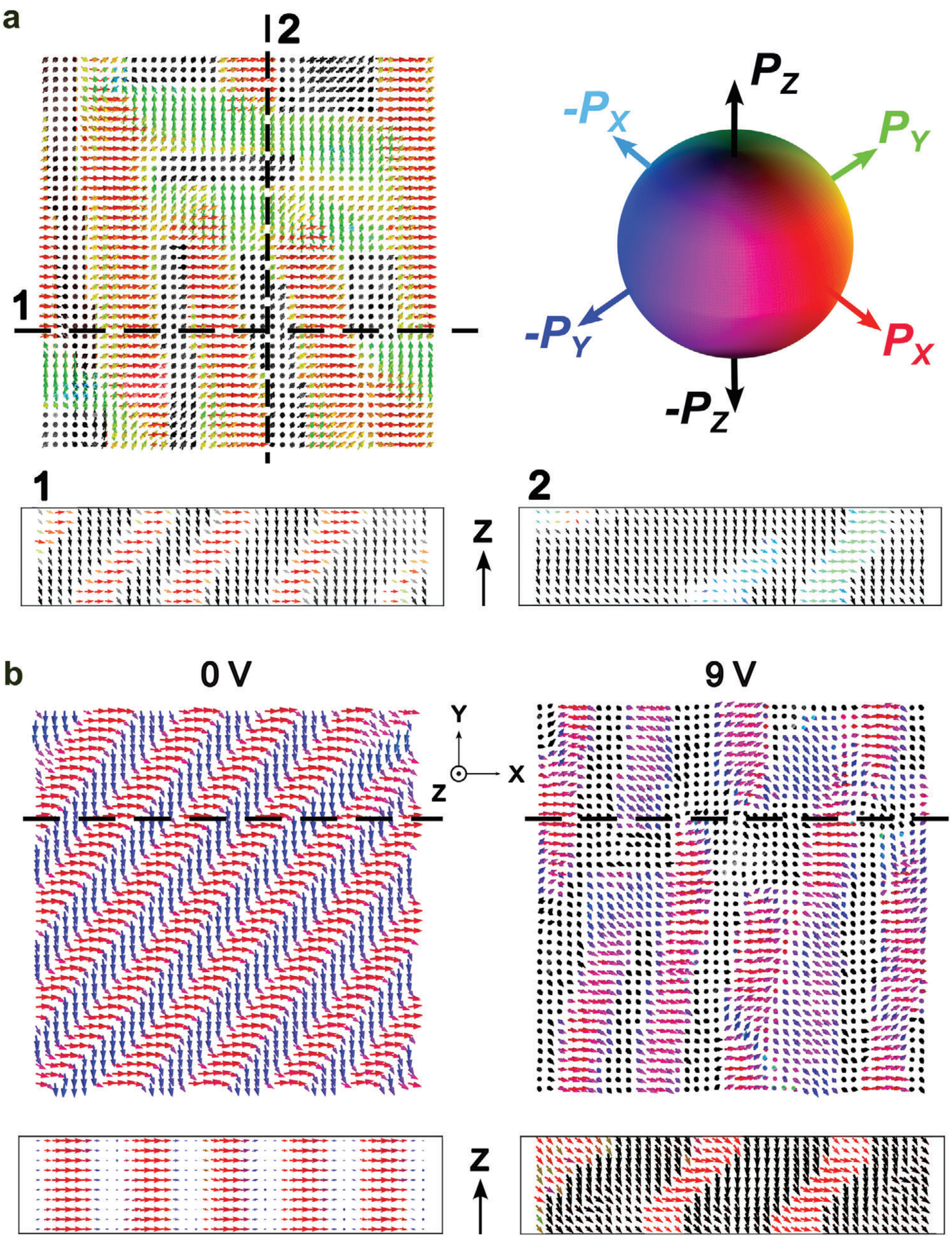

Figure 6. Phase field simulations of domain evolution under applied field. a) Domains at zero field in a $PbTiO_3$ capacitor without dielectric layers illustrating the $a_1/a_2/c$ domain structure favored by strain in the absence of depolarizing fields. b) Domains in a capacitor with $PbTiO_3$ sandwiched between two dielectric layers. At zero bias, a purely in-plane polarized a_1/a_2 domain structure is observed. Application of bias leads to nucleation of c-domains, as illustrated by the structure at 9 V, which comprises a mixture of a and c domains. Upon removal of the applied bias, the a-domain regions grow to restore the original a_1/a_2 domain state at 0 V. Each arrow represents the dipole in a single unit cell (uc) within the 10 uc x 40 uc x 40 uc simulation box.

using a different method), our results indicate that vortices are not required to obtain such permittivity values in superlattices on $DyScO_3$. Let us note also that this interpretation is consistent with the theoretical work of Graf et al.[36] Indeed, ref. [36] suggests that, as regard the out-of-plane polarization, the present superlattices can be viewed as presenting an electrostatically induced incipient ferroelectric state. Since electrostatic suppression of a polarization is the key ingredient for negative capacitance, such a (vortex-free) state is predicted to yield a negative capacitance response and a concomitant enhancement of the overall capacitance.

8. Conclusion

In conclusion, our results have two important implications. First, although the presence of negative permittivity in the ferroelectric layers cannot be directly verified, the observation of large out-of-plane permittivities in our in-plane polarized superlattices is a promising step in the realization of negative capacitance and giant voltage amplification recently predicted in electrostatically induced incipient ferroelectrics.[36] Second, although they do not possess the traditional antipolar ground state at the unit cell level, our superlattices exhibit several characteristic features of antiferroelectric materials. With respect to the out-of-plane direction, they have a macroscopically non-polar ground state that is in close proximity to a polar state (with a/c domains). This polar state can be reached with an applied field and results in the characteristic antiferroelectric double hysteresis. The paraelectric-to-ferroelectric phase transition to an in-plane polarized state is analogous to the paraelectric-to-antipolar transition of conventional antiferroelectrics. Thus, from the functional point of view, our superlattices could be considered as synthetic antiferroelectrics and provide a novel route to engineering future antiferroelectric materials.

9. Methods

Sample Growth: $PbTiO_3/SrTiO_3$ superlattices were deposited on $(110)_o$ $((001)_{pc})$ $DyScO_3$ substrates using off-axis radio- frequency (rf) magnetron sputtering. Prior to film deposition, the substrates were annealed at 1000°C in air for 2 h to form step and terrace surface structures.[47] Both $PbTiO_3$ and $SrTiO_3$ layers were grown at 550°C in a 0.18 Torr atmosphere with an argon to oxygen ratio of 28:20 with rf power of 60 W. The first and last layer of each superlattice was $SrTiO_3$, and the number of repetitions was chosen such that the total thickness is ≈70–80 nm. For some samples, $SrRuO_3$ top and bottom electrode layers (≈20 nm thick) were deposited in a 0.1 Torr atmosphere with the argon:oxygen ratio of 60:3 at an rf power of 60 W. The deposition temperatures for the top and bottom electrodes were 550 and 650°C, respectively. Average superlattice layer thicknesses were estimated from XRD data for a series with fixed $PbTiO_3$ growth time per layer and given to the nearest integer unit cell when quoting superlattice compositions.

X-Ray Diffraction: Laboratory XRD and reciprocal space mapping was carried out using a 9 kW Rigaku Smartlab system with a rotating anode and Cu Kα_1 radiation and a 2-bounce (220) Ge monochromator. The line focus optics and detector acceptance lead to the projection of reciprocal space features onto the scattering plane; therefore a_1/a_2 domain satellites along $\langle 110\rangle_{pc}$ appear as projections on the q_z-q_x reciprocal space maps.[31] Synchrotron XRD measurements were carried out at the ID01 beamline at ESRF using an incident X-ray energy of 10 keV selected using a Si(111) double crystal monochromator with resolution $\Delta\lambda/\lambda = 10^{-4}$-. Large-area RSMs (Figures 1d and 4a–c) were taken with a (300×300) μm^2 parallel beam delivering approximately 10^{11} photons/s onto the sample. Scanning X-ray diffraction microscopy (nanodiffraction) measurements (Figure 4d) were performed using a tungsten Fresnel zone plate with 300 μm diameter and 60 nm outer zone width, focusing around 10^{11} photons/s into a spot (58×55) nm^2 FWHM (full width at half maximum) in size, as measured via a ptychography scan of a known reference object. The sample was raster scanned relative to the focused beam in 55 nm steps using a commercial piezo scanner. A 2D MAXIPIX detector positioned about 40 cm downstream of the sample stage was exposed for 10 ms at each sample position. Different domain structures produce different features in reciprocal space, some of which can be captured simultaneously by appropriately positioning the 2D detector, as in Figure 4c. Here, the satellites from the periodic a_1/a_2 domains with periodicities along [110] and [1$\bar{1}$0] cut the detector plane at positions labeled as roi1 and roi2, while the lattice tilts from the a/c domain structure produce diffuse peaks at in roi7 and roi8 for the c domains and further up on the detector (not labeled) fort he a domains. With the detector position fixed, recording the intensity in each such region of interest (roi) as the sample is translated relative to the beam using a piezo-stage, allows the relative fraction of each domain variant to be mapped out as a function of lateral position on the sample.

Electrical Measurements: For in-plane electrical measurements, a gold interdigitated electrode pattern was deposited on the surface of the sample with 50 fingers, each 5 μm wide, 500 μm long, and with a spacing of 5 μm. Dielectric constant values are model dependent and sensitive to parasitic parallel capacitance contributions; hence, raw capacitance values are quoted instead.

Parallel-plate capacitor devices for out-of-plane measurements were fabricated by patterning the top $SrRuO_3$ electrode into circles with a radius of 25 μm using UV photolithography and argon-ion etching. The $SrRuO_3$ electrodes were contacted by attaching an indium wire to the top electrode and applying silver paste to the bottom electrode. Effective out-of-plane dielectric constant values were obtained from the capacitance C using $\epsilon_r = Cd/\epsilon_0 A$, where d is the thickness of the superlattice, A is the area of the electrode, and ϵ_0 is the permittivity of free space.

Electrical measurements were performed in a Janis CCS-150 closed cycle cryostat. For dielectric permittivity measurements, an Agilent E4980A precision LCR meter was used to measure the complex impedance as a function of frequency from 100 Hz to 2 MHz. The values shown in Figure 3 correspond to capacitance and tan δ measured at 1 kHz in the parallel (C_p-D) mode. For polarization hysteresis loop measurements, triangular waves of 1 kHz were applied using a Keysight 33500B waveform generator and displacement current was measured using a Keysight MSOX 3054A oscilloscope and a FEMTO DLPCA-200 current amplifier.

Scanning Transmission Electron Microscopy: The cross-section lamella for STEM imaging was prepared using a dual-beam focused ion beam integrated scanning electron microscope (Thermo-Fisher Scientific FEI G5 CX). After electron-beam deposition of C and Pt on the surface, the samples were thinned to electron transparency in four steps.[48] The STEM imaging was carried out using a Thermo-Fisher Scientific double-tilt STEM holder in the Thermo-Fisher Scientific FEI probe-corrected monochromated XFEG Spectra 300. The microscope was operated at 300 kV. The convergence angle was 31.3 mrad, and the collection angle for ADF images was 52–200 mrad using the HAADF detector. All STEM images were processed using Thermo Fisher Scientific drift corrected frame integration Velox software to correct for drift/scan distortion.

Piezoresponse Force Microscopy: A Bruker Dimension Icon microscope was used to characterize the surface topography and domain structure of the superlattices. The sample was attached to a magnetic metallic disc using silver paste, which was also applied to the side of the sample to connect the bottom electrode to the sample stage. Silicon probes (Bruker CONTV-PT) with Pt/Ir conductive coating and stiffness of 0.2 Nm^{-1} were used. During domain mapping, an AC voltage with an amplitude of 1 V peak-to-peak near the resonance frequency was applied. A DC bias was applied to the top electrode through both the AFM tip and an indium wire using a Bruker Signal Access Module, as sketched in Figure 2a. The laser spot position along the cantilever was (approximately) directly above the tip apex for Figures 2d–i and 5, and slightly further away from the free end for Figure 2b,c. In the latter case, the VPFM channel signal (not shown) was dominated by cantilever buckling effects and therefore also showed a_1/a_2 domain contrast.

Due to the parallel-plate capacitor geometry employed here, the full superlattice volume is expected to be uniformly excited by the applied field, in contrast to the near-surface excitation induced by the highly inhomogeneous fields under a PFM tip in the absence of a macroscopic top electrode. Nevertheless, nucleation of domains in the near-surface layers is expected to lead to more pronounced and better resolved changes in topography than those due to domains buried deep in the superlattice. Therefore, while these measurements are sensitive to the average piezoresponse of the whole structure, the local contrast may be dominated by the near-surface features.

PFM Image Treatment: Figure 2k is a composite image consisting of four layers prepared using data from Figure 2d–i. The data in Figure 2d,e,g,h were obtained simultaneously in a single scan. The data in Figure 2f and i were obtained simultaneously in a separate scan with the sample rotated by 90°, and were rotated accordingly to allow direct comparison. Layer 1 of the composite image consists of a greyscale image from Figure 2e. Layer 2 is a semi-transparent image consisting of VPFM amplitude data in Figure 2d, which were normalized and then thresholded to retain only values above 0.2. Layer 3 contains data from Figure 2f,i. The data from Figure 2f were normalized and thresholded to retain only values above 0.55, corresponding to the minority a_1/a_2 variants (i.e., brightest regions in Figure 2f). The thresholded array was multiplied by the normalized phase from Figure 2i. The resulting matrix was used to generate the RGB image in layer 3. Features from the topography images at 0° and 90° were used to align layer 3 relative to layer 1 and correct for differences in image distortion arising from the nonsimultaneous acquisition of the data in layers 1 and 3. Finally, layer 4 with arrows and annotations was added to indicate approximate directions of the crystallographic axes and net polarization in the superdomains.

Phase-Field Simulations: Simulations of the domain structure were performed by using the time-dependent Ginzburg–Landau equation to minimize the total free energy $F(P_i,\eta_{ij})$. To model $PbTiO_3$, the energy functional and coefficients from ref. [49] were used, to which the term $\alpha_{1122}(P_1^4P_2^4 + P_2^4P_3^4 + P_1^4P_3^4)$ with $\alpha_{1122} = 8 \times 10^9\ C^{-8}m^{14}$ was added, following ref. [50]. Further, the gradient energy coefficients were set to $G_{11} = 2.4 \times 10^{-10}\ C^{-2}m^4N$ and $G_{44} = 1.2 \times 10^{-10}\ C^{-2}m^4N$. For simplicity, the dielectric $SrTiO_3$ layers were modeled as 4 unit cell-thick gaps with a dielectric constant of 100. A 3D mesh of $10 \times 40 \times 40$ unit cells with a spacing of 0.4 nm was used for the $PbTiO_3$ layer, with periodic boundary conditions along the in-plane directions. In the out-of-plane direction, at the upper boundaries, the elastic field satisfies the zero stress condition for its normal and shear components. To mimick the effects of epitaxial strain imposed by the substrate, a moderate tensile in-plane strain of 0.2% (defined relative to the hypothetical cubic paraelectric lattice parameter of $PbTiO_3$) was imposed by fixing the average in-plane strain. All the equations were discretized using the finite difference approximation and the normalization of the energy expansion coefficients, grid spacing, and the iteration time-step follows the procedure outlined in refs. [49,50]. It is noted that the aim of this simplified model is to capture the interplay between strain, depolarization, and applied fields that lead to the observed zero-field a_1/a_2 structure and field-induced a/c structure, rather than provide a quantitative comparison with experiment.

Second-Principles Simulations: Second-principles simulations as implemented in the SCALE-UP code were run.[51–53] The atomistic models for the superlattices are based on models for bulk $SrTiO_3$ and $PbTiO_3$ described in detail in refs. [17,14]. To obtain the polarization-electric field curves, a structural optimization at each value of the field was run. The field is increased and decreased sequentially in steps of 0.5 MV cm^{-1}, and the optimized configuration of the previous field is used to start the optimization at the next value of the field.[20] The structural optimization is carried out using a Metropolis Monte Carlo simulated annealing, by which the system is given an initial temperature (100 K) and the temperature is reduced by a constant factor of 0.9975 at each Monte Carlo step.

Supporting Information

Supporting Information is available from the Wiley Online Library or from the author.

Acknowledgements

The authors acknowledge the ESRF for provision of synchrotron radiation facilities and the use of the London Centre for Nanotechnology Atomic Force Microscope Facility. This work benefited from the UK-Luxembourg bilateral EPSRC-FNR funding scheme with work at UCL supported by the EPSRC though grant. No. EP/S010769/1, and work at LIST funded by the Luxembourg National Research Fund (FNR) through grant No. INTER/RCUK/18/12601980. This project has also received funding from the European Union's Horizon 2020 research and innovation programme under grant agreement No. 964931 (TSAR).

Conflict of Interest

The authors declare no conflict of interest.

Data Availability Statement

Datasets supporting the findings of this study are available from the corresponding author upon reasonable request.

Keywords

antiferroelectricity, domains, ferroelectric superlattices

Received: March 18, 2024
Revised: July 30, 2024
Published online:

[1] K. M. Rabe, in *Functional Metal Oxides: New Science and Novel Applications*, (Eds.: S. B. Ogale, T. V. Venkatesan, M. G. Blamire), Wiley, Verlag **2013**.
[2] C. A. Randall, Z. M. Fan, I. Reaney, L. Q. Chen, S. Trolier-McKinstry, *J. Am. Ceram. Soc.* **2021**, *104*, 3775.
[3] M. E. Lines, A. M. Glass, in *Principles and Applications of Ferroelectrics and Related Materials*, Clarendon Press, Oxford, UK **1977**.
[4] K. Karda, A. Jain, C. Mouli, M. A. Alam, *Appl. Phys. Lett.* **2015**, *106*, 163501.
[5] A. S. Mischenko, Q. Zhang, J. F. Scott, R. W. Whatmore, N. D. Mathur, *Science* **2006**, *311*, 1270.
[6] P. Vales-Castro, R. Faye, M. Vellvehi, Y. Nouchokgwe, X. Perpina, J. M. Caicedo, X. Jorda, K. Roleder, D. Kajewski, A. Perez-Tomas, E. Defay, G. Catalan, *Phys. Rev. B* **2021**, *103*, 054112.
[7] M. Graf, J. Iniguez, *Commun. Mater.* **2021**, *2*, 60.
[8] J. S. Baker, M. Paściak, J. K. Shenton, P. Vales-Castro, J. H. B. Xu, P. Márton, R. G. Burkovsky, G. Catalan, A. M. Glazer, D. R. Bowler, arxiv 2021, 2102.08856.
[9] H. Aramberri, C. Cazorla, M. Stengel, J. Iniguez, *Npj Comput. Mater.* **2021**, *7*, 196.
[10] Y. Liu, R. Niu, A. Majchrowski, K. Roleder, K. Cordero-Edwards, J. M. Cairney, J. Arbiol, G. Catalan, *Phys. Rev. Lett.* **2023**, *130*, 216801.
[11] Y. L. Yao, A. Naden, M. K. Tian, S. Lisenkov, Z. Beller, A. Kumar, J. Kacher, I. Ponomareva, N. Bassiri-Gharb, *Adv. Mater.* **2023**, *35*, 2206541.
[12] Y. L. Tang, Y. L. Zhu, X. L. Ma, A. Y. Borisevich, A. N. Morozovska, E. A. Eliseev, W. Y. Wang, Y. J. Wang, Y. B. Xu, Z. D. Zhang, S. J. Pennycook, *Science* **2015**, *348*, 547.
[13] A. K. Yadav, C. T. Nelson, S. L. Hsu, Z. Hong, J. D. Clarkson, C. M. Schlepuetz, A. R. Damodaran, P. Shafer, E. Arenholz, L. R. Dedon, D. Chen, A. Vishwanath, A. M. Minor, L. Q. Chen, J. F. Scott, L. W. Martin, R. Ramesh, *Nature* **2016**, *530*, 198.
[14] S. Das, Y. L. Tang, Z. Hong, M. A. P. Goncalves, M. R. McCarter, C. Klewe, K. X. Nguyen, F. Gomez-Ortiz, P. Shafer, E. Arenholz, V. A. Stoica, S. L. Hsu, B. Wang, C. Ophus, J. F. Liu, C. T. Nelson, S. Saremi, B. Prasad, A. B. Mei, D. G. Schlom, J. Iniguez, P. Garcia-Fernandez, D. A. Muller, L. Q. Chen, J. Junquera, L. W. Martin, R. Ramesh, *Nature* **2019**, *568*, 368.
[15] V. A. Stoica, N. Laanait, C. Dai, Z. Hong, Y. Yuan, Z. Zhang, S. Lei, M. R. McCarter, A. Yadav, A. R. Damodaran, S. Das, G. A. Stone, J. Karapetrova, D. A. Walko, X. Zhang, L. W. Martin, R. Ramesh, L. Q. Chen, H. Wen, V. Gopalan, J. W. Freeland, *Nat. Mater.* **2019**, *18*, 377.
[16] M. Hadjimichael, Y. Q. Li, E. Zatterin, G. A. Chahine, M. Conroy, K. Moore, E. N. O' Connell, P. Ondrejkovic, P. Marton, J. Hlinka, U. Bangert, S. Leake, P. Zubko, *Nat. Mater.* **2021**, *20*, 495.
[17] P. Zubko, J. C. Wojdel, M. Hadjimichael, S. Fernandez-Pena, A. Sene, I. Luk'yanchuk, J. M. Triscone, J. Iniguez, *Nature* **2016**, *534*, 524.

[18] P. Zubko, N. Jecklin, N. Stucki, C. Lichtensteiger, G. Rispens, J. M. Triscone, *Ferroelectrics* **2012**, *433*, 127.
[19] E. Glazkova, K. McCash, C. M. Chang, B. K. Mani, I. Ponomareva, *Appl. Phys. Lett.* **2014**, *104*, 012909.
[20] H. Aramberri, N. S. Fedorova, J. Iniguez, *Sci. Adv.* **2022**, *8*, eabn4880.
[21] G. Rispens, B. Ziegler, Z. Zanolli, J. Iniguez, P. Ghosez, P. Paruch, *Phys. Rev. B* **2014**, *90*, 139905.
[22] B. Carcan, H. Bouyanfif, M. El Marssi, F. L. Marrec, L. Dupont, C. Davoisne, J. Wolfman, D. C. Arnold, *Adv. Mater. Interfaces* **2017**, *4*, 1601036.
[23] J. A. Mundy, B. F. Grosso, C. A. Heikes, D. F. Segedin, Z. Wang, Y. T. Shao, C. Dai, B. H. Goodge, Q. N. Meier, C. T. Nelson, B. Prasad, F. Xue, S. Ganschow, D. A. Muller, L. F. Kourkoutis, L. Q. Chen, W. D. Ratcliff, N. A. Spaldin, R. Ramesh, D. G. Schlom, *Sci. Adv.* **2022**, *8*, eabg5860.
[24] A. R. Damodaran, J. D. Clarkson, Z. Hong, H. Liu, A. K. Yadav, C. T. Nelson, S. L. Hsu, M. R. McCarter, K. D. Park, V. Kravtsov, A. Farhan, Y. Dong, Z. Cai, H. Zhou, P. Aguado-Puente, P. Garcia-Fernandez, J. Iniguez, J. Junquera, A. Scholl, M. B. Raschke, L. Q. Chen, D. D. Fong, R. Ramesh, L. W. Martin, *Nat. Mater.* **2017**, *16*, 1003.
[25] A. K. Yadav, K. X. Nguyen, Z. J. Hong, P. Garcia-Fernandez, P. Aguado-Puente, C. T. Nelson, S. Das, B. Prasad, D. Kwon, S. Cheema, A. I. Khan, C. M. Hu, J. Iniguez, J. Junquera, L. Q. Chen, D. A. Muller, R. Ramesh, S. Salahuddin, *Nature* **2019**, *565*, 468.
[26] Z. J. Hong, A. R. Damodaran, F. Xue, S. L. Hsu, J. Britson, A. K. Yadav, C. T. Nelson, J. J. Wang, J. F. Scott, L. W. Martin, R. Ramesh, L. Q. Chen, *Nano Lett.* **2017**, *17*, 2246.
[27] C. B. Tan, Y. Q. Dong, Y. W. Sun, C. Liu, P. Chen, X. L. Zhong, R. X. Zhu, M. W. Liu, J. M. Zhang, J. B. Wang, K. H. Liu, X. D. Bai, D. P. Yu, X. P. Ouyang, J. Wang, P. Gao, Z. L. Luo, J. Y. Li, *Nat. Commun.* **2021**, *12*, 4620.
[28] M. J. Hytch, E. Snoeck, R. Kilaas, *Ultramicroscopy* **1998**, *74*, 131.
[29] J. D. Budai, M. F. Chisholm, R. Feenstra, D. H. Lowndes, D. P. Norton, L. A. Boatner, D. K. Christen, *Appl. Phys. Lett.* **1991**, *58*, 2174.
[30] S. L. Morelhao, J. Z. Domagala, *J. Appl. Crystallogr.* **2007**, *40*, 546.
[31] A. S. Everhardt, S. Matzen, N. Domingo, G. Catalan, B. Noheda, *Adv. Electron. Mater.* **2016**, *2*, 1500214.
[32] Y. J. Wang, Y. P. Feng, Y. L. Zhu, Y. L. Tang, L. X. Yang, M. J. Zou, W. R. Geng, M. J. Han, X. W. Guo, B. Wu, X. L. Ma, *Nat. Mater.* **2020**, *19*, 881.
[33] H. Lu, Y. Tan, L. Richarz, J. He, B. Wang, D. Meier, L.-Q. Chen, A. Gruverman, *Adv. Funct. Mater.* **2023**, *33*, 2213684.
[34] E. K. H. Salje, O. Aktas, M. A. Carpenter, V. V. Laguta, J. F. Scott, *Phys. Rev. Lett.* **2013**, 111, 247603.
[35] G. Catalan, A. Lubk, A. H. G. Vlooswijk, E. Snoeck, C. Magen, A. Janssens, G. Rispens, G. Rijnders, D. H. A. Blank, B. Noheda, *Nat. Mater.* **2011**, *10*, 963.
[36] M. Graf, H. Aramberri, P. Zubko, J. Iniguez, *Nat. Mater.* **2022**, *21*, 1252.
[37] W. J. Merz, *Phys. Rev.* **1953**, *90*, 375.
[38] M. I. Morozov, D. Damjanovic, *J. Appl. Phys.* **2008**, *104*, 034107.
[39] S. Liu, R. E. Cohen, *Appl. Phys. Lett.* **2017**, *111*, 082903.
[40] V. G. Koukhar, N. A. Pertsev, R. Waser, *Phys. Rev. B* **2001**, *64*, 214103.
[41] A. R. Damodaran, S. Pandya, J. C. Agar, Y. Cao, R. K. Vasudevan, R. J. Xu, S. Saremi, Q. Li, J. Kim, M. R. McCarter, L. R. Dedon, T. Angsten, N. Balke, S. Jesse, M. Asta, S. V. Kalinin, L. W. Martin, *Adv. Mater.* **2017**, *29*, 1702069.
[42] X. Y. Lu, Z. H. Chen, Y. Cao, Y. L. Tang, R. J. Xu, S. Saremi, Z. Zhang, L. You, Y. Q. Dong, S. Das, H. B. Zhang, L. M. Zheng, H. P. Wu, W. M. Lv, G. Q. Xie, X. J. Liu, J. Y. Li, L. Chen, L. Q. Chen, W. W. Cao, L. W. Martin, *Nat. Commun.* **2019**, *10*, 3951.
[43] E. Langenberg, H. Paik, E. H. Smith, H. P. Nair, I. Hanke, S. Ganschow, G. Catalan, N. Domingo, D. G. Schlom, *ACS Appl. Mater. Inter.* **2020**, *12*, 20691.
[44] P. Shan, J. J. Xiong, Z. J. Wang, C. He, X. M. Yang, R. B. Su, X. F. Long, *J. Mater. Chem. C* **2020**, *8*, 6654.
[45] J. Ge, D. Remiens, X. L. Dong, Y. Chen, J. Costecalde, F. Gao, F. Cao, G. S. Wang, *Appl. Phys. Lett.* **2014**, *105*, 112908.
[46] J. H. Haeni, P. Irvin, W. Chang, R. Uecker, P. Reiche, Y. L. Li, S. Choudhury, W. Tian, M. E. Hawley, B. Craigo, A. K. Tagantsev, X. Q. Pan, S. K. Streiffer, L. Q. Chen, S. W. Kirchoefer, J. Levy, D. G. Schlom, *Nature* **2004**, *430*, 758.
[47] J. E. Kleibeuker, G. Koster, W. Siemons, D. Dubbink, B. Kuiper, J. L. Blok, C. H. Yang, J. Ravichandran, R. Ramesh, J. E. ten Elshof, D. H. A. Blank, G. Rijnders, *Adv. Funct. Mater.* **2010**, *20*, 3490.
[48] Y. Q. Li, E. Zatterin, M. Conroy, A. Pylypets, F. Borodavka, A. Bjorling, D. J. Groenendijk, E. Lesne, A. J. Clancy, M. Hadjimichael, D. Kepaptsoglou, Q. M. Ramasse, A. D. Caviglia, J. Hlinka, U. Bangert, S. J. Leake, P. Zubko, *Adv. Mater.* **2022**, *34*, 2106826.
[49] Y. L. Li, S. Y. Hu, Z. K. Liu, L. Q. Chen, *Acta Mater.* **2002**, *50*, 395.
[50] W. Zhang, K. Bhattacharya, *Acta Mater.* **2005**, *53*, 185.
[51] J. C. Wojdel, P. Hermet, M. P. Ljungberg, P. Ghosez, J. Iniguez, *J. Phys.-Condens. Mat.* **2013**, *25*, 305401.
[52] P. Garcia-Fernandez, J. C. Wojdel, J. Iniguez, J. Junquera, *Phys. Rev. B* **2016**, *93*, 195137.
[53] C. Escorihuela-Sayalero, J. C. Wojdel, J. Iniguez, *Phys. Rev. B* **2017**, *95*, 094115.